Natural Hazards (2025) 121:8995–9020
https://doi.org/10.1007/s11069-025-07164-9

ORIGINAL PAPER

Stability analysis and prediction of Bimslope failures using numerical modelling and hybrid meta-heuristic models

Arunava Ray[1] · Gopika C. Atul[2] · Sanjog Chhetri Sapkota[3] · Prasenjit Saha[4] · Sourav Das[5] · Rajesh Rai[6] · Manoj Khandelwal[7]

Received: 3 September 2024 / Accepted: 28 January 2025 / Published online: 10 February 2025

Abstract
Bimsoil slope (Bimslope) or Soil-Rock-Mixture slopes are complex geological formations made up of geotechnically important 'blocks' enclosed in a finer-textured 'matrix.' These geomaterials possess heterogeneous properties owing to changes in the block and matrix properties that can arise from natural weathering processes or various anthropogenic activities. The present study focuses on the stability analysis of a Bimslope under varying block properties (orientation and volumetric block proportion), matrix type (Loamy sand, Sandy loam, and Silt loam) and matrix water content. The study indicates that the failure of a Bimslope is not governed by only one physical parameter but rather by a critical combination of block properties, matrix type and matrix water content. When the water content (< 25% saturation) and block content (< 25%) are less, the failure is governed by matrix only. With the increase in block content, the failure is governed by block however under fully saturated (100% saturation) conditions, the failure is solely governed by matrix type irrespective of block properties. In addition to that, the data generated using numerical analysis was used to predict the factor of safety using hybridized ensembled methods considering the XGB model and three other novel meta-heuristic algorithms (MHA): political optimization (POA), the Leopard Seal algorithm (LSA), and the Giant Armadillo Algorithm (GAA). It has been found that among all the models, the GAA-XGB algorithm exhibits better results with R^2 and RMSE values as 0.99628, 0.055436 in training and 0.985664, 0.063092 in the testing stage. Furthermore, SHAP-based analysis has been performed to identify the most influential parameters.

Keywords Bimslope · Soil-rock-mixture · Saturation · Nature inspired algorithm · SHAP analysis

1 Introduction

'Bimsoil' or 'Soil-Rock Mixtures' refer to several frequently occurring geological units that have a 'block-in-matrix' fabric and are referred to as "geotechnically complex formations" (Fig. 1). This geological formation possesses a variable characteristic significantly different from pure rock mass or soil mass (Medley 1994; Wakabayashi and Medley 2004;

Extended author information available on the last page of the article

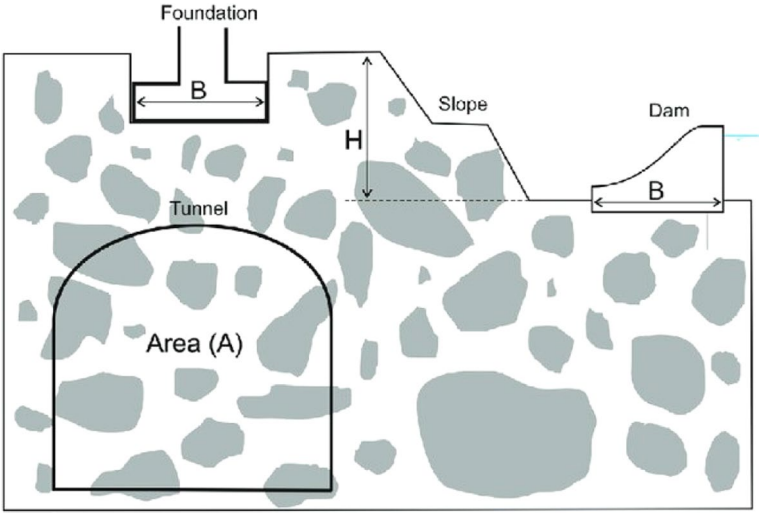

Fig. 1 Bimsoil formation encountered during various engineering works (Sonmez et al. 2016)

Napoli et al. 2022). While both Bimsoil and Soil-Rock Mixtures (SRMs) involve a combination of soil and rock materials, there are distinct differences between the two. SRMs encompass a broader range of materials with varying degrees of soil and rock content and a wider range of mechanical behaviours. While both Bimsoil and SRMs involve a combination of soil and rock materials, Bimsoil is a specific type of SRM, characterized by a distinct block-in-matrix structure with a weaker soil matrix and larger rock blocks. Block Size is typically larger in the case of Bimsoil while it can vary widely, from fine-grained particles to larger boulders for SRMs. Also, the Block-Matrix Interaction is weak or no bonding in the case of Bimsoil while it can range from weak to strong bonding in SRMs (Medley 1994).

In the last decade, several studies have been conducted to identify factors affecting these complex formations' mechanical behaviour (Sonmez et al. 2006; Afifipour and Moarefvand 2014; Barbero et al. 2012; Napoli et al. 2021). These studies indicate that the durability, deformability, and failure mechanism of these geomaterials is significantly influenced by Volumetric Block Proportion (VBP), which is the volume of the rocks (or blocks) present related to the volume of the matrix (or soil) (Afifipour and Moarefvand 2014; Napoli et al. 2021; Barbero et al. 2012; Sonmez et al. 2006). Several authors (Kalender et al. 2014; Khorasani et al. 2019; Li et al. 2013; Mahdevari and Maarefvand 2016) have also emphasized the significance of other block parameters, such as the block's shape, dimensions, and alignment, on the mechanical response of these complex geological formations.

Bimsoil formations that occur in slope, it is called Bimslope (Khorasani et al. 2019). Afifipour and Moarefvand (2014); Napoli et al. (2021); Barbero et al. (2012); and Sonmez et al. (2006) while working with laboratory scale Bimslope model, concluded that the behaviour and characteristics of the Bimslope can be considerably influenced by its VBP. When the VBP is between 25 and 75%, the failure path of the Bimslope often zigzags through the matrix and around the blocks. In the case of Bimslope with VBP less than 25%, it behaves more like a soil (matrix) slope whereas, Bimslope with VBP more than 75%, behaves more like a highly fractured rock slope. This was further validated by

numerical analysis performed by Afifipour and Moarefvand (2014). Khorasani et al. (2019) investigated the effect of rock block inclinations on the stability of Bimslope and the findings revealed that the inclination of the blocks has a significant impact on the safety factor and stability of the slope. Xian-Wen et al. (2020) suggested that angular rocks contributed almost three times as much to the ultimate loading of soil-rock slopes as round rocks, an effect possible because of their more complex distribution characteristics. Owing to the natural weathering process and unplanned anthropogenic activity, Bimslope behaves as a highly heterogeneous slope (Afifipour and Moarefvand 2014). The rocks (commonly called blocks) within the soil matrix can vary in shape, size, and spatial distribution. Similarly, the soil (commonly called a matrix) consists of smaller, finer particles such as soil, sand or clay that bind the blocks together. The matrix properties and strength also vary based on the degree of weathering and the presence of water. All these uncertainties in the mechanical, geographical, and geological character make the prediction of Bimslope engineering behaviour challenging (Pan et al. 2008; Napoli et al. 2021).

According to the available literature, detailed research has been done on the effect of block properties (VBP, block size, spatial distribution, orientation, density, and strength) on the stability of Bimslope. Limited work has been done to study the effect of matrix properties and matrix moisture content on the behaviour of Bimslope. The critical combination of block properties, matrix strength, and the presence of water largely governs the failure in Bimslope geological formations. Understanding the combined effect of these parameters is crucial for accurately predicting Bimslope behaviour and the development of landslide remedial measures. This study utilizes laboratory investigations combined with numerical analysis to provide valuable insight into the complex behaviour of Bimslope under the combined effect of block properties, matrix properties, and matrix moisture content. Furthermore, the data generated using numerical analysis was used to predict the factor of safety using hybridized ensembled methods considering the XGB model and three other novel meta-heuristic algorithms (MHA): political optimization (POA), the Leopard Seal algorithm (LSA), and the Giant Armadillo Algorithm (GAA). The use of recently developed metaheuristic algorithms to tune the hyperparameters of ensemble models. Additionally, this study utilizes several SHAP-based sensitivity analyses that provide substantial insights into input–output relationships.

2 Materials and properties

Ray et al. (2023) performed a detailed geotechnical study on the residual soil derived from the weathering of Carbonate (Limestone and Dolomite) lithologies in the Lesser Himalayan region of the Indian states of Uttarakhand and Himachal Pradesh. Based on the detailed literature study, ten locations were selected for sample collection. The GPS locations of the selected sites have been marked on Google Maps using a handheld GPS apparatus (Ray et al. 2023). Representative disturbed and undisturbed soil and rock samples were collected from all the sites to perform laboratory tests and to develop a theoretical Bimslope model that was analyzed numerically in the present study.

2.1 Geotechnical investigation of the soil/matrix

The soil (matrix) part was separated from the soil-rock mixture, and sieve analysis and specific gravity tests were performed. It was observed that the average clay fraction varies

from 1.5 to 3.6%, the average silt fraction varies mainly from 10.7 to 17.2%, the average fine sand fraction varies mainly from 11.3 to 22.0%, the average medium sand fraction varies mainly from 19.2 to 28.6%, average coarse sand fraction varies mainly from 11 to 23% and the average gravel fraction varies mainly from 4.0 to 12.3%. It was identified that the residual soil from the study area contains an average of 82.6% of coarse aggregate (gravel and sand) and the rest of 17.4% of fine aggregates (silt and clay) which are mostly well-graded (since C_u is > 3 for all samples). The range of the effective size (D_{10}) varies from 0.02 to 0.07 mm indicating the sandy nature and high permeability of the soil. Based on the Unified Soil Classification system, the soil of the study area is classified as silty clay of low plasticity (CL and CL-ML) with a significant amount of gravel and sand. The detail of sieve analysis for samples collected from all the ten sites is given in Ray et al. (2023). The natural water content varies between 6.6% and 28.0% with an average of around 14%. The sieve analysis helped in separating soil particles of different size ranges (sand i.e., particles with a size between 4.75 mm and 75 microns and fine i.e., particles with a size < 75 microns). Three different types of remoulded soil (matrix) samples were prepared, as shown in Table 1, using the separated soil particles from sieve analysis. This is done to incorporate the time-dependent weathering effect in the slope. Due to weathering (physical as well as chemical), the share of fine particles keeps on increasing over a period of time. Thus, studying the effect of different compositions of the matrix will help in developing a better understanding of the Bimslope at different times. The clay fraction in the actual soil sample collected from the site was much less (< 3.5%). Thus, for the testing purpose in this study, clay content of 5%, 15% and 25% of the Fine fraction (silt + clay) was utilised for the Loamy sand matrix, Sandy loam matrix and Silt loam matrix respectively. The clay fraction was increased gradually to incorporate the time-dependent weathering impact.

In the field, soil saturation levels vary and are determined by climatic conditions, drainage conditions, porosity, particle density, and other factors affecting soil shear strength (Müller et al. 2016; Tyagi et al. 2013; Ray et al. 2021). If the air volume is small, the soil may become saturated under stress. If the air content is very high, the soil remains unsaturated and experiences significant volume changes even in undrained conditions. As a result, it is critical to understand the relationship between varying water content and soil shear strength in partially saturated to saturated soils in terms of total stress. Thus, Consolidated-Undrained (CU) triaxial tests are performed on several samples with a predetermined level of initial saturation. Tables 2, 3, 4 show the average engineering properties of the remoulded samples collected from different sites of carbonate lithologies.

2.2 Geotechnical investigation of the rock/block

A series of triaxial, Brazilian tensile, Poisson's ratio and specific gravity tests were performed according to ISRM's suggested method using the rock samples collected from the

Table 1 Different types of remoulded matrix samples according to USDA soil textural classification prepared for the study

Sand (%)	Fine (%)	Remoulded sample classification
80	20	Loamy sand
60	40	Sandy loam
30	70	Silt loam

Table 2 Engineering properties of Loamy sand matrix with various degrees of initial saturation percentages

Properties	0% saturation	25–35% saturation	50–60% saturation	75–85% saturation	95–100% saturation
Cohesion (kPa)	4.5	16.5	27.5	16.0	13.0
Friction angle (degree)	39.0	36.0	30.0	30.5	22.5
Young modulus (MPa)	98.5	94.0	92.5	77.5	50.5
Unit weight (kN/m^3)	16.1	16.1	15.9	15.8	15.7

Table 3 Engineering properties of Sandy loam matrix with various degrees of initial saturation percentages

Properties	0% saturation	25–35% saturation	50–60% saturation	75–85% saturation	95–100% saturation
Cohesion (kPa)	5.0	22.5	32.0	27.5	22.5
Friction angle (degree)	35.5	31.5	28.0	25.0	21.0
Young modulus (MPa)	94.0	85.5	79.5	62.0	47.5
Unit weight (kN/m^3)	16.4	16.2	16.2	16.1	15.9

Table 4 Engineering properties of Silt loam matrix with various degrees of initial saturation percentages

Properties	0% saturation	25–35% saturation	50–60% saturation	75–85% saturation	95–100% saturation
Cohesion (kPa)	7.5	27.5	38.5	29.5	24.5
Friction angle (degree)	28.0	22.0	18.5	15.5	13.5
Young modulus (MPa)	74.5	63.5	52.5	41.5	30.5
Unit weight (kN/m^3)	17.2	17.2	17.0	16.9	16.8

sites. Before testing, the rock core samples were prepared from the samples collected from the sites. The Young's modulus for the corresponding samples was obtained through the stress–strain curve obtained from the triaxial test. The details about rock sampling and testing process in the laboratory are given in Ray et al. (2023). The average value of each rock strength parameter was taken for the numerical analysis (Table 5).

3 Numerical analysis

The data obtained from laboratory investigations has been used to develop several numerical models to study the behaviour of a simulated Bimslope under varying VBP (25%, 35%, 45%, and 55%), Rock/Block orientation (0°, 20°, 40°, 60°, and 150° from horizontal), Soil/Matrix types (Loamy sand, Sandy loam, and Silt loam) and Soil saturation level (5 saturation levels) of matrix. The numerical analysis was performed using Finite Element Software Phase^2 8.0 to study the deformation, failure pattern and Factor of Safety (FoS) Bimslope. Overall, 300 numerical models were created and analyzed. The basic slope model used for analysis is shown in Fig. 2a. The blocks (rock) present in the sites were mostly rectangular and slender in shape with sharp edges, with few being cylindrical (Fig. 2b). Thus, to generalise a common and uniform size

Table 5 Geotechnical parameters of tested rock samples (dry)

Site	Cohesion (MPa)	Friction angle (degree)	Young's modulus (GPa)	Tensile strength (MPa)	Poisson's ratio	Specific gravity
1	14	22	40	10	0.33	2.64
2	17	23	51	13	0.26	2.74
3	16	32	47	12	0.33	2.72
4	13	39	59	9	0.34	2.86
5	11	30	48	7	0.17	2.67
6	15	32	38	9	0.19	2.69
7	17	45	59	11	0.33	2.85
8	19	32	52	10	0.28	2.84
9	13	27	44	9	0.23	2.63
10	15	37	32	10	0.31	2.73

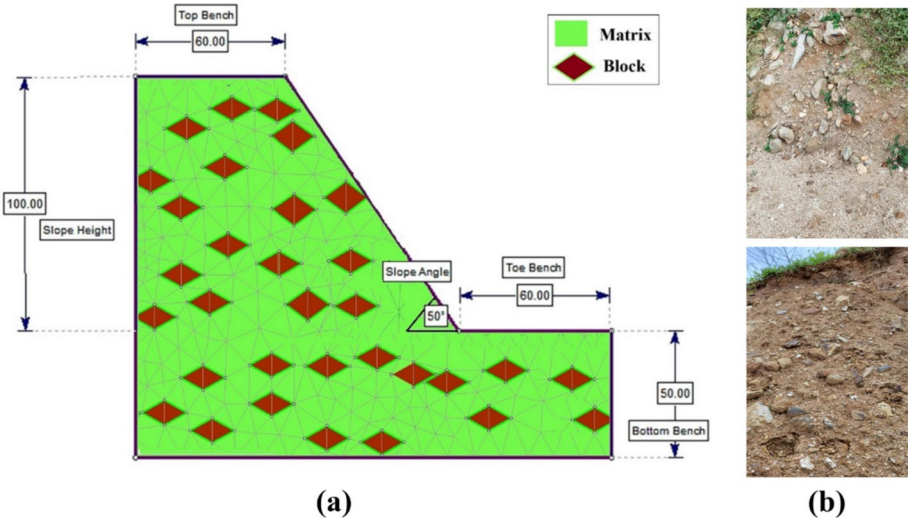

Fig. 2 **a** Basic model of a Bimslope developed for numerical analysis and **b** Shapes of blocks in study areas

block shape (rhombus) was selected for the study. The spatial distribution of the rock blocks (according to the respective VBPs) within the slope is carried out using MATLAB code. Also, the majority of the blocks were in the size range 10–25 cm (the maximum size was around 85 cm). Thus, the developed MATLAB code was designed in such a way to generate multiple blocks of the size following a log-normal distribution with a mean of 15 cm and a standard deviation of 5. The data obtained through numerical analysis will be used further for developing various machine learning algorithms that can effectively predict the behaviour of Bimslope.

4 AI-based methodology

This section explores the working methodology with a detailed overview of applied soft computing models for assessing the factor of safety. The successful application of advanced machine learning techniques in geotechnical engineering has been demonstrated in studies by Khandelwal and Singh (2011), Monjezi et al. (2014), Parsajoo et al. (2021), Ke et al. (2021), and Zhou et al. (2022). Additionally, several investigations, including those by Rahul et al. (2015), Asteris et al. (2022), and Zhang et al. (2022), have utilized various machine-learning models to assess slope stability. In this study hybridized ensembled methods considering the XGB model and three other novel meta-heuristic algorithms (MHA): political optimization (POA) (Askari et al. 2020), the Leopard Seal algorithm (LSA) (Rabie et al. 2023), and the Giant Armadillo Algorithm (GAA) (Alsayyed et al. 2023) have been used. A detailed overview of applied models is presented in Fig. 3. The consequent section provides a comprehensive explanation of each of the models.

4.1 XGBoost algorithm (XGB)

Extreme Gradient Boosting (XGBoost) is a machine learning algorithm that has gained popularity for its high performance. This algorithm is classified as an ensemble machine learning method that can be applied to both regression and classification tasks (Bentéjac et al. 2021). XGBoost can be employed as an advanced gradient-boosting technique that leverages distributed or parallel processing capabilities. This learning algorithm is considered reliable due to its incorporation of two self-compatible functions, namely column subsampling and shrinkage. Furthermore, in the case of a large dataset, this technique exhibits reduced computational time and improved predictive performance compared to the gradient boosting technique. This technique exhibits the capacity for effective problem-solving with minimal resource demands. In this study, the XGBoost algorithm was employed to investigate the overall potential of boosting techniques.

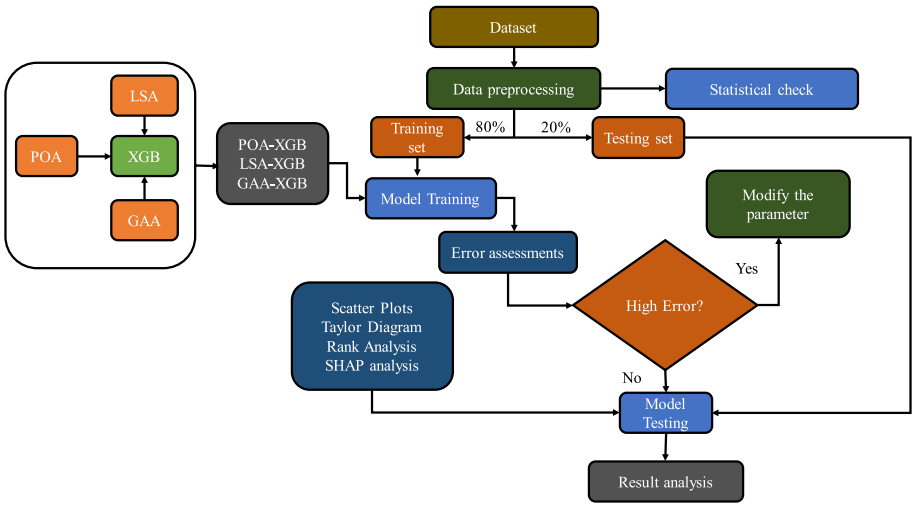

Fig. 3 Working methodology of the study

XGBoost, like Gradient Boosting, constructs an additive enhancement of the objective function through the minimization of a loss function (Chen and Guestrin 2016). XGBoost, being a machine learning algorithm, employs decision trees exclusively as base predictive models. A modified version of the loss function is employed to regulate the complexity of these trees, as shown in Eqs. (1) and (2).

$$L_{xgb} = \sum_{i=1}^{N} L\left(y_i, F(x_i)\right) + \sum_{m=1}^{M} \Omega\left(h_m\right) \tag{1}$$

$$\Omega(h) = \gamma T + \frac{1}{2}\lambda \|w\|^2 \tag{2}$$

where T indicates the total tree leaves count, w shows the output scores indicated with those leaves. L is the loss function used in the study, γ is the factor to control the hyperparameters.

4.2 Optimization algorithm

4.2.1 Political optimizer algorithm (POA)

Political optimization algorithm (POA) is a recently developed global optimization algorithm inspired by the multi-phased procedure involved in politics (Askari et al 2020). It is a mathematical illustration of the essential aspects of politics, including the distribution of constituencies, party affiliations, election campaigns, internal party elections, and constitutional activities. The process involves optimization from two perspectives: each party seeks to enhance its reputation to secure victory in the election, and each party strives to maximize its parliamentary seats to establish a governing body. Initially, a political party member can be seen as a candidate solution. Subsequently, the goodwill of an individual is equivalent to the position of the candidate solution in the search space. Finally, the performance-related parameters that define the goodwill of a political member can be imitated by design variables or components of the position vector of a candidate solution.

$$\mathcal{P} = \left\{\mathcal{P}_1, \mathcal{P}_2, \mathcal{P}_3, \ldots, \mathcal{P}_{\mathrm{n}}\right\} \tag{3}$$

$$P_i = \left\{p_i^1, p_i^2, p_i^3, \ldots, p_i^n\right\} \tag{4}$$

$$p_i^j = \left[p_{i,1}^j, p_{i,2}^j, p_{i,3}^j, \ldots, p_{i,d}^j\right]^T \tag{5}$$

where, the entire population P is split in n number of political parties, as shown in Eq. (3). Each Party P_i consists of n candidates/members, as shown in Eq. (4) in which p_i^1 is taken as a potential solution, which is a d-dimensional vector, as shown in Eq. (5). The value of d is the number of input variables of the problem being solved and $p_{i,k}^j$ denotes kth dimension of p_i^j. The potential solution $p_{i,k}^j$ is considered a party member and an election candidate.

The best-fit member of a party is selected as the party leader, decided after the inter-party election. The Party selection process is modelled in Eq. (6), where p_i^* denotes the leader of the ith party and $f(p_i^j)$ is for computes its fitness.

$$q = \underset{1 \le j \le n}{\operatorname{argmin}} f\left(p_i^n\right), \forall i \in \{1, \ldots, n\} \tag{6}$$

This phase runs after the election campaign where each member p_i^j is selected with probability λ and switched to some randomly selected party P_r, where it is swapped with the least fit member p_r^q of the party P_r. The computation of the index q for the least fit member of P_r is expressed in Eq. (7).

$$q = \underset{1 \le j \le n}{\operatorname{argmin}} f\left(p_r^n\right) \tag{7}$$

4.2.2 Leopard seal algorithm (LSA)

Leopard Seal Optimization (LSO) is a newly developed optimization algorithm that draws inspiration from leopard seals' foraging behaviour (Rabie et al 2023). They remain continuously attentive in pursuit of prey, irrespective of their hunger state. Their conduct illustrates that they engage in self-distribution by allocating a distinct search range to each individual. When a member of the seal herd discovers prey, the remaining members assemble in the vicinity and launch a coordinated attack. The LSO model consists of three consecutive phases: (I) prey search, (II) prey encirclement, and (III) prey assault. As described in the following section, these stages quantitatively represent the lion seals' predation dominance.

The position vectors of leopard seals during their movement in each cycle, denoted by ξ, are maintained properly. The initial point of SA of the ith cycle ($\vec{X}_{init}^{j}$) is known beforehand as it indicates the ending point of spiral in (i-1)th iteration, which can also be denoted by $\vec{X}_{\xi}^{i-1}$. $\vec{X}_{1}^{i}$ and $\vec{X}_{\xi}^{i}$ denote the start and end point of the current and ith iteration respectively. During each search phase iteration, ξ position vectors of roaming leopard seals are denoted as $\vec{X}_{p}^{i} \forall p \in \{1, 2, 3, \ldots, \xi\}$ and the objective function's value is $F(\vec{X}_{p}^{i}) \forall p \in \{1, 2, 3, \ldots, \xi\}$. The ξ position vectors of ith iteration of seal L_m is calculated by:

$$\vec{X}_{\alpha}^{i}\left(L_m\right) | \forall \alpha \in 1, 2, 3, \ldots, \xi - 1 = \vec{D}^{i}\left(L_m\right) \cdot e^{bf_{\alpha}} \cos\left(2\pi f_{\alpha}\right) + \vec{X}_{\xi}^{i} L_m \tag{8}$$

where $\vec{X}_{\alpha}^{i}\left(L_m\right)$ is the new α's position of L_m at final ith iteration and $\vec{D}^{i}\left(L_m\right)$ is the distance between the leopard seal and its prey.

The second phase is for the encirclement of the prey, in which the search agent curbs the prey and finds the optimal solution. The prime hindrance of this phase is that the position of the prey is not pre-known, hence the need to allocate the prey's position beforehand. Single-leader prey Allocation (SLPA) is the simplest method for the allocation of prey. Based on SLPA, the prey's position is demonstrated as:

$$\vec{X}_{prey} = Position\left[\begin{matrix} argmax\_Validation\left[F\left(L_m\right)\right] \\ \forall L_m \in S \end{matrix}\right] \tag{9}$$

where S are search agents sets and $F\left(L_m\right)$ is a fitness function for the LSO algorithm. Another method is Multi Leader Prey Allocation (MLPA). If there are k leaders in z-dimensional space, the position vector of *i*th leader can be denoted as: $\vec{X}_i = \left[x_{1i}, x_{2i}, x_{3i} \ldots .., x_{zi}\right]$. The prey's predicted position can be represented by:

$$\vec{X}_{prey} = \frac{1}{k}\begin{pmatrix} \sum_{i=1}^{k} x_{1i} \\ \sum_{i=1}^{k} x_{2i} \\ \cdots \\ \cdots \\ \cdots \\ \sum_{i=1}^{k} x_{zi} \end{pmatrix} \tag{10}$$

Though effective, MLPA is not accurate if the location of prey is very close to one seal (leader) and very far from other seals. To overcome this defect, Weighted Leaders Prey Allocation (WLPA) is used where selected leaders are assigned a weight based on their distance from prey with an assigned weight w_i. Then the prey's predicted position can be represented by:

$$\vec{X}_{prey} = \frac{1}{\sum_{m=1}^{k} W(L_m)}\begin{pmatrix} \sum_{m=1}^{k} W(L_m).x_{1m} \\ \sum_{m=1}^{k} W(L_m).x_{2m} \\ \cdots \\ \cdots \\ \cdots \\ \sum_{m=1}^{k} W(L_m).x_{zm} \end{pmatrix} \tag{11}$$

When the prey is encircled and cannot move further, the agents come nearer the prey and eventually capture them. The distance between the agent and the prey $\left(\vec{D}^{i}_{L_m}\right)$ in this phase is calculated by:

$$\vec{D}^{i}_{L_m} = \left|\vec{X}^{i}_{prey} - \vec{X}^{i}_{L_m}\right| \tag{12}$$

4.2.3 Giant armadillo algorithm (GAA)

The Giant Armadillo Optimization (GAA) is a newly developed algorithm inspired by the hunting behaviour and strategical approach to target termite mounds by Giant Armadillos (Alsayyed et al 2023). This metaheuristic optimization algorithm combines swarm-based and population-based approaches and is divided into two phases. The first phase involves exploration, simulating Giant Armadillos' movement towards termite mounds. The second phase, exploitation, simulates the digging skills of Giant Armadillos to open the mounds and prey on the termites. The values of the decision variables are initialized using Eq. (13) based on the initial position of Giant Armadillos in the matrix space form shown in Eq. (14).

$$x_{i,d} = lb_d + r \cdot \left(ub_d - lb_d\right) \tag{13}$$

$$X = \begin{bmatrix} X_1 \\ \vdots \\ X_i \\ \vdots \\ X_N \end{bmatrix}_{N\times m} = \begin{bmatrix} x_{1,1} & \cdots & x_{1,d} & \cdots & x_{1,m} \\ \vdots & \ddots & & \iddots & \vdots \\ x_{i,1} & \cdots & x_{i,d} & \cdots & x_{i,m} \\ \vdots & \iddots & \vdots & \ddots & \vdots \\ x_{N,1} & \cdots & x_{N,d} & \cdots & x_{N\times m} \end{bmatrix}_{N\times m} \tag{14}$$

where X denotes the population matrix of GAO, X_i is the ith position state of GAO member. $x_{i,d}$ is the dth search space dimension, N is the total number of giant armadillos, m is the number of variables, r denotes random number space in the interval [0,1], lb_d and ub_d indicate the lower and upper bound of the dth variable, respectively.

For each candidate solution presented by the position of Giant Armadillo, a value for objective function is to be evaluated by using Eq. (15).

$$F = \begin{bmatrix} F_1 \\ \vdots \\ F_i \\ \vdots \\ F_N \end{bmatrix}_{N\times 1} = \begin{bmatrix} F(X_1) \\ \vdots \\ F(X_i) \\ \vdots \\ F(X_N) \end{bmatrix}_{N\times 1} \tag{15}$$

Here, F and F_i are the vector of the objective function and the objective function for the ith GAO member respectively.

The set of such locations for each member is shown in Eq. (16). The new position is randomly updated to one of the condition termite mounds from the set of candidate termite mounds and attacked using Eq. (17).

$$TM_i = \left\{X_k : F_k < F_i and k \neq i\right\}, \quad where\ i = 1, 2, \ldots, N\ and\ k \in \{1, 2, \ldots, N\} \tag{16}$$

Here, TM_i is the location for the ith giant armadillo for the set of candidate termite mounds', X_k is the total population member with optimal objective function value than the ith giant armadillo, and F_k is its adopted objective function value.

$$x_{i,j}^{P1} = x_{i,j} + r_{i,j} \cdot \left(STM_{i,j} - I_{i,j} \cdot x_{i,j}\right) \tag{17}$$

$$X_i = \begin{cases} X_i^{P1}, & F_i^{P1} < F_i, \\ X_i, & else \end{cases} \tag{18}$$

Here, STM_i is the adopted termite mound for ith giant armadillo, $STM_{i,j}$ is its jth dimension, X_i^{P1} is the updated position calculated for the ith giant armadillo. The attacking phase of the proposed GAO, $x_{i,j}^{P1}$ is its jth dimension, F_i^{P1} is its objective function value, $r_{i,j}$ are arbitrary numbers from the interval [0, 1], and $I_{i,j}$ are numbers that are arbitrarily selected.

In the exploitation phase, the digging action of a giant armadillo to open the mound and prey on the termites is modelled. It results in minor changes in the position of the giant armadillo. Thus, it increases the exploitation of the algorithm in the local search space. Thus, a new position calculated based on Eq. (19) is changed by the initial position of the member according to Eq. (20) where the value of the objective function is enhanced.

$$x_{i,j}^{P2} = x_{i,j} + \left(1 - 2r_{i,j}\right) \cdot \frac{ub_j - lb_j}{t} \tag{19}$$

$$X_i = \begin{cases} X_i^{P2}, & F_i^{P2} < F_i, \\ X_i, & else \end{cases} \tag{20}$$

Here, X_i^{P2} is the updated position calculated for the ith giant armadillo on the digging phase of the proposed GAO, $x_{i,j}^{P2}$ is the jth dimension, F_i^{P2} is its optimized objective function value, $r_{i,j}$ are the arbitrary numbers from the [0, 1] interval, and t is the total iteration.

Table 6 Statistical parameters of input and output features

Features	Nomenclature	Count	Mean	Median	Min	Max	Std. Deviation
Input parameters							
Volumetric block proportion	VBP	300	40	40	25	55	11.18034
Rock/block orientation	RO	300	54.3	40	0	150	52.29254
Soil/matrix type	ST	300	2	2	1	3	0.816497
Soil/matrix saturation	SS	300	50	50	0	100	35.35534
Output parameters							
Factor of safety	FoS	300	1.32	1.07	0.34	6.57	0.847772

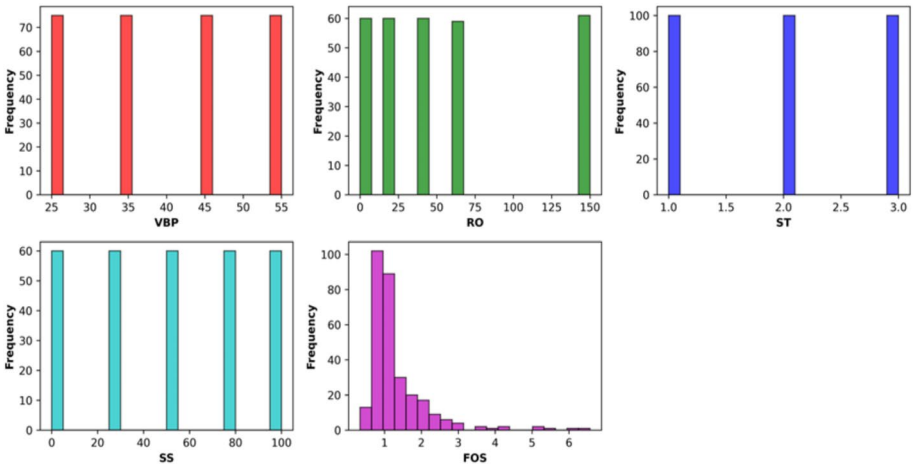

Fig. 4 Histogram plot of input and output features

4.3 Descriptive details and statistical explanation

The performance of the models for predicting the Factor of Safety (FoS) generally depends on the quality and the quantity of the datasets adopted. So, a robust framework is needed to unveil the intricate relationships between the input and the output features. The statistical summary of the influential features is presented in Table 6. In addition, the histogram of the experimental dataset is provided in Fig. 4. It represents the frequency-based histogram along with the distribution. It shows that the data are unevenly distributed along the different ranges for each feature. The statistical Pearson correlations between the target (y) and the feature (x) are displayed in Fig. 5. The coefficient ranges from − 1 to 1, where 0 indicates no correlation. A value closer to 1 demonstrates a more significant positive correlation; in contrast, a closer to − 1 expresses a greater negative correlation. It can be observed that it has a very weak correlation between factor safety and other input variables. Despite their usefulness for initial data analysis, statistical correlations fail to capture the combinatorial non-linear connections between the multivariate x and y, which are crucial for machine learning-based research.

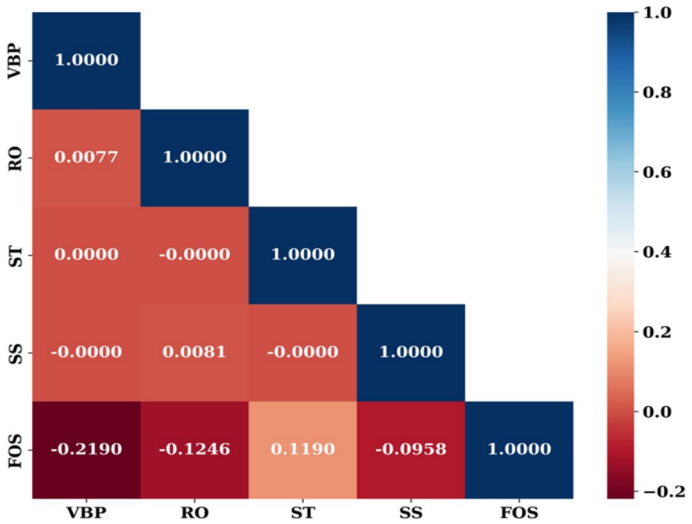

Fig. 5 Pearson correlation plot of input and output features

4.4 Performance measure

To evaluate the model's efficacy, different statistical parameters such as the Mean Absolute Error (MAE), Root Mean Square Error (RMSE), Mean Square Error (MSE), and Coefficient of Determination (R^2) have been used (Ray et al. 2020; Verma et al. 2023; Paliwal et al. 2022; Nandy et al. 2024; Bharati et al. 2022). The equation of different statistical measures is mentioned below. The MAPE, MAE, and RMSE values near zero indicate a good performance model. The R^2 values approaching 1, indicate higher predicting efficiency, whereas the value near zero indicates less efficiency. The equation of different statistical measures is mentioned below.

$$R^2 = \frac{\left[\sum_{i=1}^{n}(t_i - \bar{t})(y_i - \bar{y}\right]}{\left[\sum_{i=1}^{n}\left(t_i - \bar{t}\right)^2\right]\left[\sum_{i=1}^{n}\left(p_i - \bar{p}\right)^2\right]} \tag{21}$$

$$RMSE = \sqrt{\frac{1}{n}\sum_{i=1}^{n}(t_i - y_i)^2} \tag{22}$$

$$MAE = \frac{1}{n}\sum_{i=1}^{n}|t_i - y_i| \tag{23}$$

$$MSE = \frac{1}{n}\sum_{i=1}^{n}(t_i - y_i)^2 \tag{24}$$

N = number of data samples, t_i and y_i are predicted value and actual value, and $\bar{t}$ and $\bar{y}$ are the average predicted and actual values respectively.

4.5 Hyperparameter tuning and cross-validation

In the present study, the entire dataset is arbitrarily divided into training and testing datasets. The model has been trained using 90% of the dataset; the remaining 10% has been utilized for model testing (Lyngdoh et al. 2022). Subsequently, the training set underwent fivefold cross-validation; this involved partitioning the training set into 5 sets. Finally, the models' average performance is presented in Table 7. Hyperparameters are parameters that can impact the model's performance directly. Therefore, it is important to adjust these hyperparameters. The hyperparameter range is crucial for figuring out the optimal hyperparameter values. Table 7 contains a tabulation of the hyperparameter space and the optimal hyperparameters of the various algorithms employed for the output parameter. The current study uses XGB as a primary model and three novel meta-heuristic algorithms (MHA): political optimization (POA), the Leopard Seal algorithm (LSA), and the Giant Armadillo Algorithm (GAA). The XGB model and MHA hybridization are POA-XGB, LAS-XGB, and GAA-XGB. The optimization algorithm is used to tune XGB hyperparameters by setting three hyperparameters of XGB: learning rate, max_depth, and n_estimators (Karir et al. 2022). All the optimized hyperparameters are tabulated in Table 7. The cost function used in this study is Mean Squared Error (MSE). This study utilizes a problem space with a dimensionality (dim) of 3. The maximum number of iterations (max_iter) is set to 100. The POA is set with n_population of 20, divided into five parties, distributing 20 per cent of the total population. The population_size is set as 20 for GAA. The LSA with a probability of moving the seal towards the best individual (p_move) is set as 0.7, and p_seal with step size for leopard seal movement is set as 0.1. n_population with 50 is used to develop the hybridized model.

5 Result and discussion

5.1 Numerical analysis

Figures 6, 7, 8 show the variation of Bimslope FoS with VBP for different rock orientations and matrix saturation levels when the matrix type changes from Loamy sand, Sandy loam and Silt loam respectively.

Table 7 Optimal hyperparameters

Model names	Hyperparameters specifications	Optimal combination
POA-XGB	learning_rate (0.1 to 1)	0.85
	max_depth (5 to 20)	9
	n_estimators (10 to 200)	88
LSA-XGB	learning_rate (0.1 to 1)	0.3
	max_depth (5 to 20)	4
	n_estimators (10 to 200)	165
GAA-XGB	learning_rate (0.1 to 1)	0.63
	max_depth (5 to 20)	11
	n_estimators (10 to 200)	190

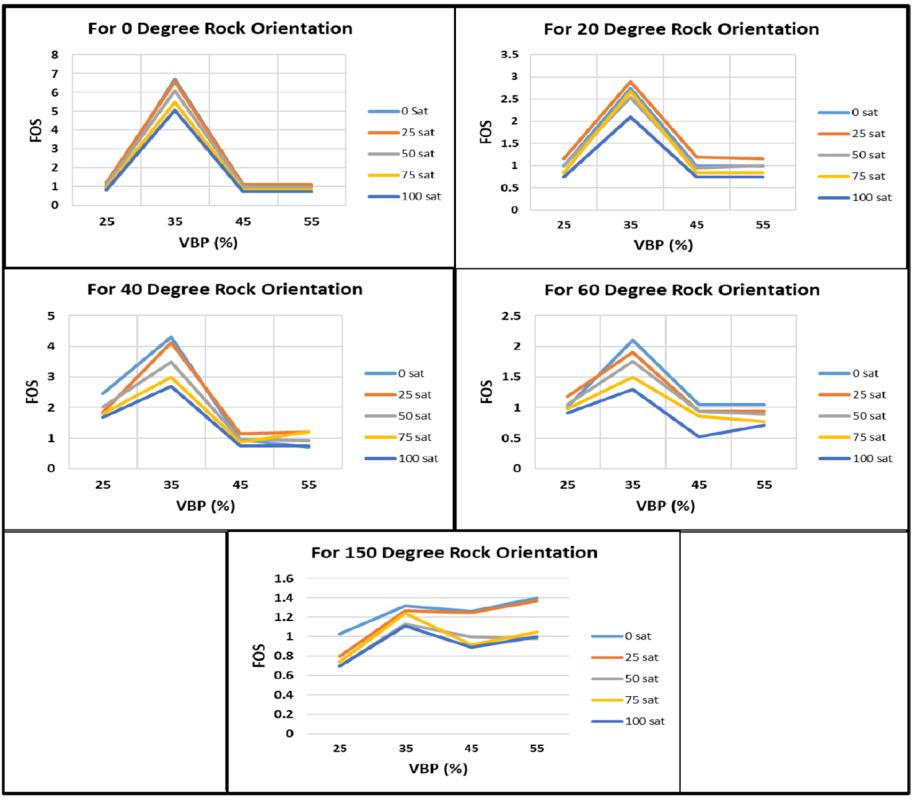

Fig. 6 Variation of Bimslope FoS with VBP for different rock orientations and matrix saturation levels in Loamy sand matrix

5.1.1 Effect of different types of soil on the factor of safety

It is observed that the FoS is decreasing in the case of Sandy loam and Silty loam compared to that of Loamy sand. This is because the loamy sand has got higher percentage of sand and a lower percentage of silt. Generally, soils with higher sand content tend to increase the shear strength of soil due to frictional resistance between the sand particles. This can lead to higher safety factors. Sandy loam and Silty Loam have a greater percentage of silt, and soils with higher percentages tend to have lower shear strength compared to sandy soil. Due to this, the two soils show lower FoS compared to Sandy Loam.

5.1.2 Effect of saturation on the factor of safety

The results obtained show that the FoS decreases with an increase in the degree of saturation in all types of soil. This is because the presence of water in the pores of a soil-rock mixture tends to reduce the effective stress acting between the particles, leading to lower shear strength. This ultimately leads to a decrease in the FoS with an increase in the degree of saturation.

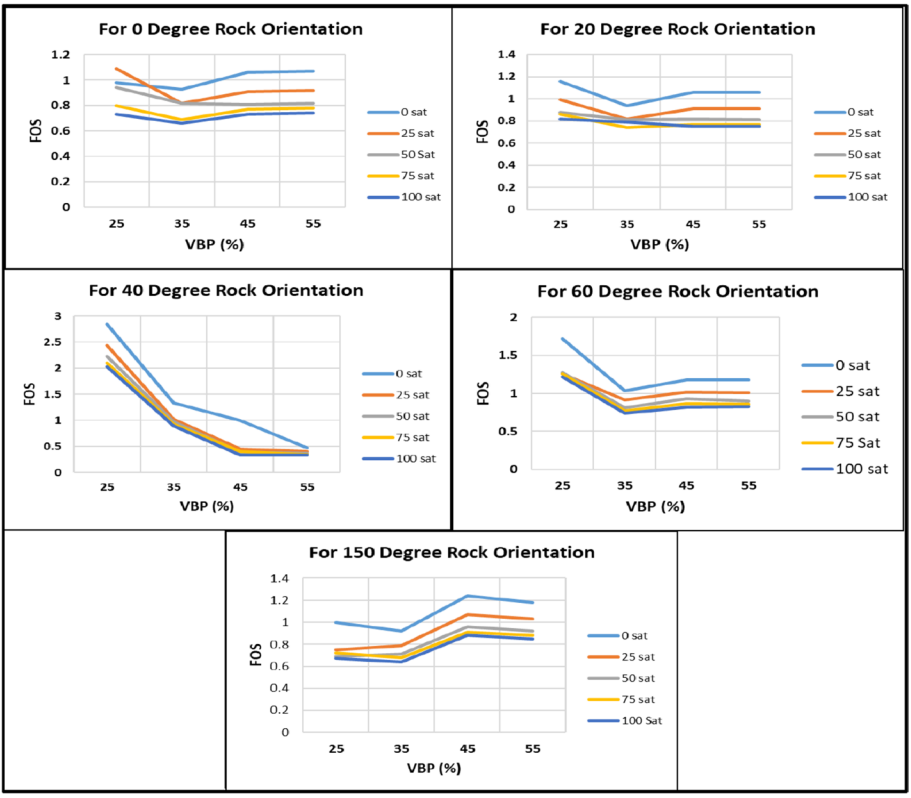

Fig. 7 Variation of Bimslope FoS with VBP for different rock orientations and matrix saturation levels in Sandy loam matrix

5.1.3 Effect of VBP on the factor of safety

From the results obtained for Loamy sand, it is seen that the FoS is increasing with an increase in VBP from 25 to 35% and thereafter decreasing with an increase in VBP up to 55% for all the degrees of saturation. This may be because initially when the VBP increases there is an enhancement of the overall mechanical properties of Bimslope which leads to an increase in the factor of safety. But as the VBP increases the number of contact points between the blocks increases, and these connections are weak which results in a decrease in the overall strength of rock mass. Therefore, the decrease in FoS can be seen with the increase in VBP.

For Sandy Loam and Silt Loam, the results differ from that of Loamy sand, the FoS decreases with an increase in VBP from 25 to 35% and increases with an increase in VBP up to 55%. This might be because the Sandy Loam and Silt Loam contain more silt content than Loamy sand. Initially, Sandy Loam and Silt Loam derive their shear strength from the cohesion of silt particles, later when VBP of 25% is introduced, the blocks in the matrix decrease the cohesion due to the overall accumulation of interfaces within the material. This shows the decrease in FoS initially. Further, when the VBP is increased there is a higher proportion of intact rock blocks within the Bimslope

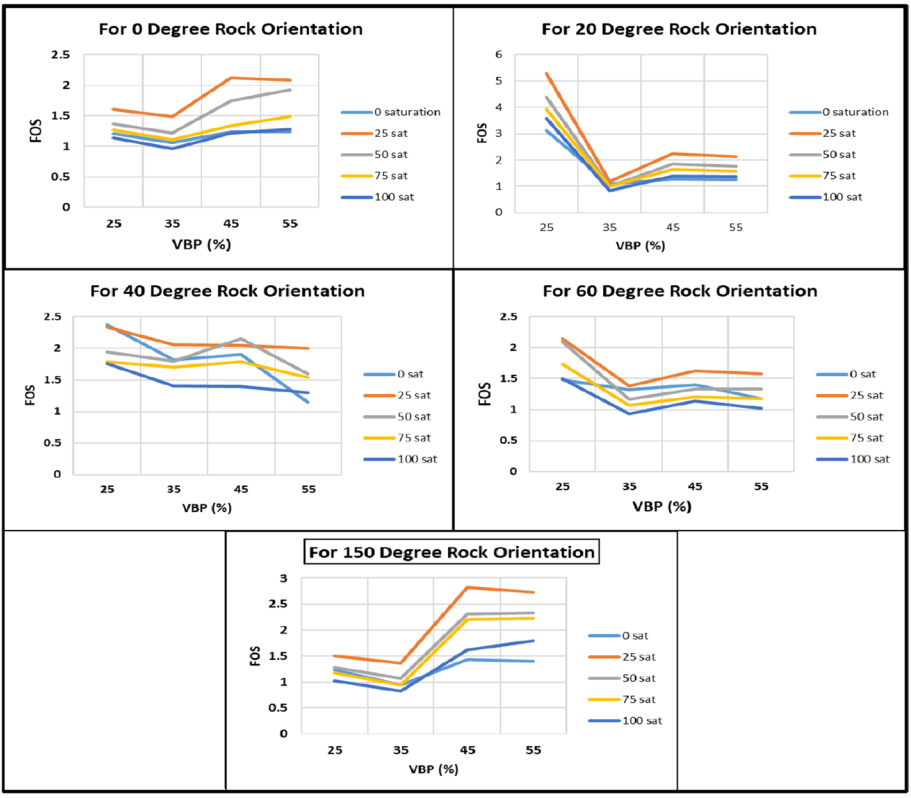

Fig. 8 Variation of Bimslope FoS with VBP for different rock orientations and matrix saturation levels in Silt loam matrix

mass, and the overall shear strength tends to increase. This is because intact rock blocks typically have higher strength and resistance to shear deformation. Therefore, the FoS increases with an increase in VBP from 35 to 45%. When VBP is increased from 45 to 55% the FoS again tends to decrease because of an increase in the number of contact points which are weak in nature.

5.1.4 Effect of block orientation on FoS

From the results it is observed that the FoS is increasing with an increase in the orientation angle up to 40° this is because as the orientation is increasing the blocks act perpendicular to the failure surface. Due to this perpendicularity, the failure surface intersects the blocks and does not proceed further thus increasing the strength of the slope. When the orientation of blocks exceeds 40° the blocks align in the direction of the slope and act almost parallel to the sloping surface (the slope angle was fixed at 50°) due to which the failure surface penetrates further and the slope starts losing its strength thus leading to decrease in the FoS.

5.1.5 Failure modes

Unlike regular slopes, Bimslopes have different failure modes because of their intricate geological makeup, which consists of strong blocks embedded in a weaker matrix. The development of tortuous slip surfaces that evade the larger blocks is the most frequent failure mechanism, and it frequently results in rotational failures. The relative strengths and weaknesses of the blocks and matrix will determine whether these slip surfaces start along the contact interfaces or within the matrix material. Numerical simulation indicates an increase in the tortuous length of the failure surface resulting from the increase in VBP. Thus, the FoS of the slope increases with the increase in VBP. Also, the orientation of the block affects the formation and shape of the tortuous failure surface. When the blocks are perpendicular to the slope surface, the tortuosity increases, while it decreases when the orientation of the blocks is parallel to the slope surface. Thus, resulting in higher FoS in the former case. The strength contrast between the blocks and the matrix material also has a major impact on the stability of Bimslopes. The Unconfined Compression Strength (UCS) test on only matrix samples indicates that the Loamy sand matrix has the highest strength followed by the Silt loam matrix and Sandy loam matrix. When the Bimslopes were analysed with the three matrices and blocks included, the highest FoS were observed for the Bimslope having Loamy sand matrix while the Bimslope with Silt loam and Sandy loam matrix has lesser FoS but are comparable with each other. Numerical analysis indicated the yielding has happened mostly shear in nature and very few in tension. Also, the shear-yielded elements are located inside the slope body while the tension yielding happens near the top and slope face.

5.2 Prediction performance of the adopted ML models

A model with a low error value and a high R^2 value statistically indicates a strong predictive performance. Several statistical metrics, such as R^2, RMSE, MAE, and MSE, are presented quantitatively in this work and are determined for the training and testing phases. It has been observed from Table 8 that, when it came to the predicting factor of safety during the training phase, the GAA-XGB model performed better than other models with statistical metrics like $R^2 = 0.99628$, RMSE = 0.055436, MAE = 0.01338. On the other hand, it has been understood that in the testing phase GAA-XGB algorithm exhibits better results with $R^2 = 0.985664$, RMSE = 0.06309, MAE = 0.0294. The accuracy of each model in predicting the factor of safety for the training and testing dataset is presented in Fig. 9.

Table 8 Performance of employed model for factor of safety

Dataset	Algorithm	R^2 score	RMSE	MAE	WI	VAF	RSR
Training set	POA-XGB	0.917379	0.261476	0.185163	0.976166	91.73792	0.287438
	LSA-XGB	0.950387	0.202622	0.127883	0.985056	95.03865	0.222741
	GAA-XGB	0.996286	0.055436	0.013383	0.99909	99.62863	0.06094
Testing set	POA-XGB	0.867744	0.191633	0.1409	0.964021	86.77436	0.363671
	LSA-XGB	0.919701	0.149319	0.112267	0.977709	91.97009	0.283371
	GAA-XGB	0.985664	0.063092	0.0294	0.996449	98.56639	0.119733

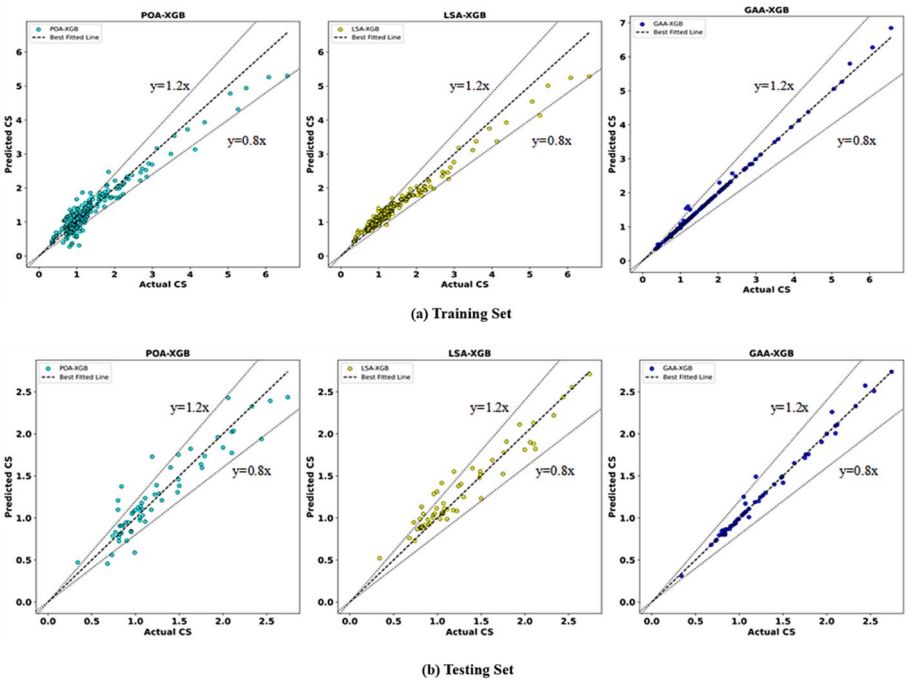

Fig. 9 Machine learning analysis **a** Training set and **b** Testing set for factor of safety

5.2.1 Taylor diagram

A Taylor diagram is a visual tool for evaluating many computational models according to how well they forecast a given dataset (Taylor 2005). The primary use of the Taylor diagram is to show, clearly and straightforwardly, how closely each model's forecasted data and actual data coincide. With the help of standard deviation (SD), RMSE, and correlation coefficient (R), the Taylor diagram gives a visual representation of the performance exhibited by a model. Figure 10 shows the Taylor diagrams for the training and testing stages for

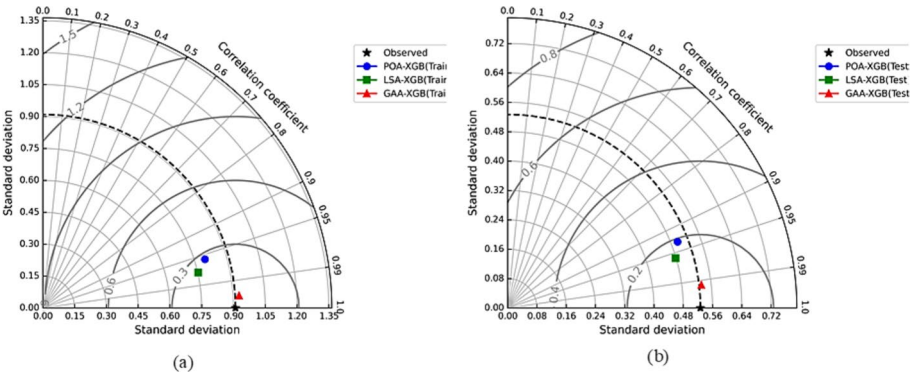

Fig. 10 Taylor diagram for factor of safety in training and testing set

the factor of safety. It has been observed that compared to the other models used, the GAA-XGB models are among the most accurate prediction models considering training and testing phases; they are found nearer the reference point. In the training set of Factor of safety, as shown in Fig. 10a, the S.D value of 73.67 for GAA-XGB is seen nearer to the reference observed S.D of 75.36, with the value of R as 0.9994. Similarly, in a testing set of Factor of safety, the reference actual set S.D is 86.32, and the R-value is 0.9917, represented in Fig. 10b. This suggests that the model's correlation and variability suit the observed data well.

5.2.2 Model Explainability using SHAP

SHAP is one of the innovative methods for deciphering model explanations by offering data insights (Lundberg et al. 2018, 2019, 2020) It incorporates the concept of Shapley values from game theory. Further, several researchers use the SHAP approach to comprehend the behaviour and correlation between the data gathered by models. This study makes use of a variety of plot formats, including summary and feature significance plots. The importance of the characteristics in the testing sets is shown in Fig. 11. ST receives the highest weight of 0.29 (32.95%) in testing sets, while VBP receives the next most weightage of 0.24 (27.27%). Likewise, RO and SS have respective weights of 0.2 (22.73%) and 0.15 (17.05%).

SHAP summary plots help illustrate global interpretations of the plot. This plot effectively offers feature attribution for each characteristic, which explains the importance of each attribute and its influence on the prediction. The x-axis represents the individual SHAP value, while the y-axis organizes the qualities based on their importance. A greater SHAP value indicates that the model predicts an enhanced safety factor. Conversely, a negative SHAP value suggests the model is trying to decrease the safety estimate factor. It is essential to acknowledge that alterations in colour correspond to modifications in the SHAP value and the characteristics used in the model's output. The analysis demonstrates that ST, VBP, RO, and SS are the primary factors that substantially impact the expected magnitude of the outcome. With the increase of ST value, there is a shift from blue to red

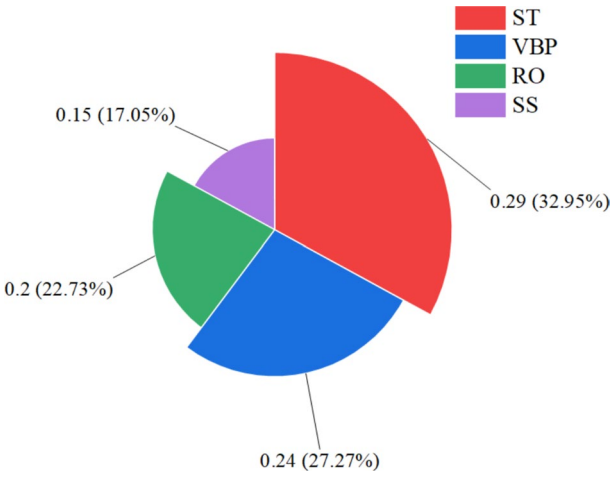

Fig. 11 Feature importance plots

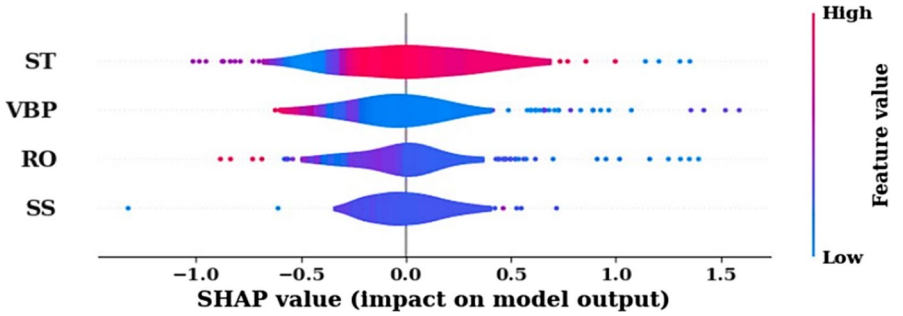

Fig. 12 SHAP summary plot

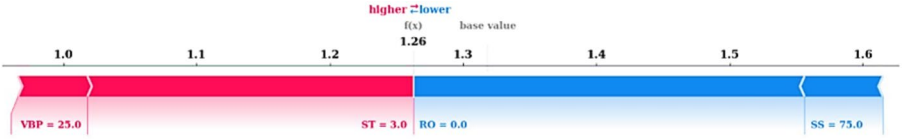

Fig. 13 Force plot

gradation colour i.e. from negative to positive indication of feature influence is higher for ST (Fig. 12).

Global interpretability intends to explain the overall behaviour shown by models. However, it does not effectively clarify the unique contributions made by various characteristics. It can be efficiently and coherently stated via local interpretability. This study employs force plots for local explanation, whereas interaction plots are compelling for local and global interpretation. The force plot for predicting FOS reveals that the VBP and ST positively influence the models, whereas the other characteristics cause the model to move toward the lower side. The RO does not influence SHAP analysis. All other features cause the output value to decrease from 1.32 (the original base value) to 1.26, as shown in Fig. 13. It indicates that the RO is not adequately captured; however, SS, ST, and VBP are accurately represented, similar to other plots.

The influence of different input parameters on the output parameter is interpreted and illustrated using the SHAP dependency plot in Fig. 14. Dependency plots illustrate the link between input and output variables by looking at the SHAP values following model assessment. The feature dependence plots for the GAA-XGB model demonstrate that the model has correctly captured the relationship among the variables. The horizontal axis in the plot corresponds to the feature value, while the vertical axis represents the SHAP values associated with the specific features. Negative shape values indicate a decreasing effect of certain features on the model's output prediction. This implies that the output values decrease as the feature values increase or vice versa. On the other hand, positive SHAP values indicate a positive correlation between the feature values and the corresponding output values, suggesting that as the feature values increase, the output values increase, and vice versa. The colour coding (from blue to red) corresponds to the interaction of the second feature with the plotted feature. From Fig. 14a it can be observed that a higher factor of safety (FoS > 1) is achieved when VBP is between 25 and 35, with relatively low values of rock orientation (RO < 30°). This also tallies with the results of the numerical analysis

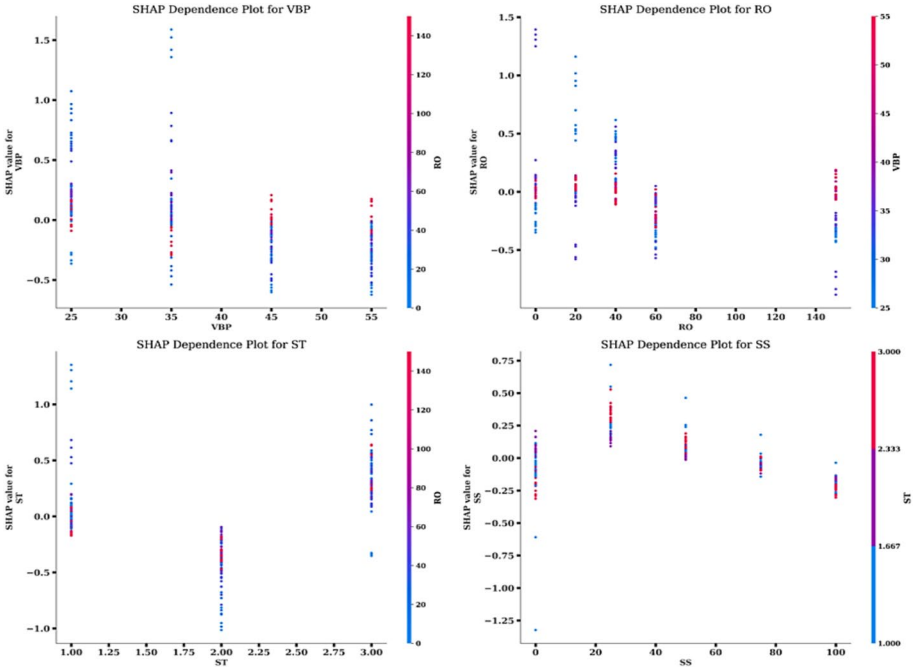

Fig. 14 SHAP interaction plots

presented in Sect. 5.1. SHAP dependence plot for RO in Fig. 14b demonstrates a decreasing trend in FoS with an increase in rock orientation. Also, FoS is higher when RO < 30° and VBP < 40%. Figure 14c shows that the highest FoS is achieved for type I soil (Loamy sand matrix), and the least for type II soil (Sandy loam matrix), with lower values of rock orientation (RO < 40°). Figure 14d demonstrates a downward trend of FoS with an increase in soil saturation, which also validates the analytical results.

6 Conclusions

Bimslopes are a typical geological formation that behaves neither like pure soil nor pure rock. Studies related to the engineering behaviour of Bimslope are limited to only variation in block properties while neglecting some important slope physical parameters like the matrix properties and water content. The current work presents a detailed numerical investigation of a Bimslope under varying block properties, matrix type and matrix water content. It further includes the utilisation of hybridized ensembled methods to assess the factor of safety of the stability of Bimslope. The machine learning model used in this current work are XGB model and three other novel meta-heuristic algorithms (MHA): political optimization (POA), the Leopard Seal algorithm (LSA), and the Giant Armadillo Algorithm (GAA). The optimization algorithm is used to tune XGB hyperparameters which results in a model with the best performance. The present investigation leads to the following findings:

- The blocks are oriented parallel to the slope angle, which has significantly less safety factor. While the orientation of the block perpendicular to the slope face provides maximum safety.
- When increasing the VBP, makes the failure path more tortuous and thus increases the safety factor and slope stability. Additionally, the factor of safety is reduced by increasing the moisture content.
- When the water content (< 25% saturation) and block content (< 25%) are less, the failure is governed by matrix only. With the increase in block content, the failure is governed by block however under fully saturated (100% saturation) conditions, the failure is solely governed by matrix type irrespective of block properties.
- Among different types of matrixes, the Silty loam matrix has the maximum factor of safety compared to Sandy loam and Loamy sand matrix Bimslope.
- The failure in Bimslope is not only dependent on the block properties, as suggested by past reviews. Rather it depends on the critical combination of water, matrix, and block properties.
- This study indicates that ensembled ML techniques are very effective in predicting the Factor of safety for the stability of Bimslope.
- Among these three considered models, the GAA-XGB algorithm exhibits better results with R^2 and RMSE values as 0.99628, 0.055436 in training and 0.985664, 0.063092 in the testing stage.
- The SHAP analysis used in this study reveals that soil/matrix type has the maximum importance/effect on FoS followed by VBP, Block orientation and Matrix water content.

Funding Open Access funding enabled and organized by CAUL and its Member Institutions. The authors have not disclosed any funding.

Declarations

Conflict of interest The authors have not disclosed any competing interests.

Ethical approval Hereby, all the authors consciously assure that: This material is the authors' own original work, which has not been previously published elsewhere. The paper is not currently being considered for publication elsewhere. The paper reflects the author's own research and analysis in a truthful and complete manner. The results are appropriately placed in the context of prior and existing research.

References

Afifipour M, Moarefvand P (2014) Experimental study of post-peak behavior of Bimrocks with high rock block proportions. J Central South Univ 21(2):761–767

Alsayyed O, Hamadneh T, Al-Tarawneh H, Alqudah M, Gochhait S, Leonova I, Dehghani M (2023) Giant Armadillo optimization: a new bio-inspired metaheuristic algorithm for solving optimization problems. Biomimetics 8(8):619

Askari Q, Younas I, Saeed M (2020) Political optimizer: a novel socio-inspired meta-heuristic for global optimization. Knowl-Based Syst 195:105709

Asteris PG, Rizal FIM, Koopialipoor M, Roussis PC, Ferentinou M, Armaghani DJ, Gordan B (2022) Slope stability classification under seismic conditions using several tree-based intelligent techniques. Appl Sci 12(3):1753

Barbero M, Bonini M, Borri-Brunetto M (2012) Numerical simulations of compressive tests on Bimrock. Electron J Geotech Eng 17:3397–3414

Bentéjac C, Csörgő A, Martínez-Muñoz G (2021) A comparative analysis of gradient boosting algorithms. Artif Intell Rev 54:1937–1967

Bharati AK, Ray A, Khandelwal M, Rai R, Jaiswal A (2022) Stability evaluation of dump slope using artificial neural network and multiple regression. Eng Comput 38(Suppl 3):1835–1843

Chen T, Guestrin C (2016) Xgboost: a scalable tree boosting system. In: Proceedings of the 22nd acm sigkdd international conference on knowledge discovery and data mining, pp 785–794

Kalender A, Sonmez H, Medley E, Tunusluoglu C, Kasapoglu KE (2014) An approach to predicting the overall strengths of unwelded Bimrocks and bimsoils. Eng Geol 183:65–79

Karir D, Ray A, Bharati AK, Chaturvedi U, Rai R, Khandelwal M (2022) Stability prediction of a natural and man-made slope using various machine learning algorithms. Transp Geotech 34:100745

Ke B, Khandelwal M, Asteris PG, Skentou AD, Mamou A, Armaghani DJ (2021) Rock-burst occurrence prediction based on optimized Naïve Bayes models. IEEE Access 9:91347–91360

Khandelwal M, Singh TN (2011) Predicting elastic properties of schistose rocks from unconfined strength using intelligent approach. Arab J Geosci 4(3–4):435–442

Khorasani E, Amini M, Hossaini MF (2019) Effect of large blocks position on stability analysis of block-in-matrix slopes. J Min Environ 10(2):465–477

Li Y, Huang R, Chan LS, Chen J (2013) Effects of particle shape on shear strength of clay-gravel mixture. KSCE J Civ Eng 17(4):712–717

Lundberg SM, Erion G, Chen H, DeGrave A, Prutkin JM, Nair B, Katz R, Himmelfarb J, Bansal N, Lee S-I (2020) From local explanations to global understanding with explainable AI for trees. Nat Mach Intell 2(1):56–67

Lundberg SM, Erion GG, Lee SI (2018) Consistent individualized feature attribution for tree ensembles. arXiv preprint arXiv:1802.03888

Lundberg SM, Erion G, Chen H, DeGrave A, Prutkin JM, Nair B, Lee SI (2019) Explainable AI for trees: from local explanations to global understanding. arXiv preprint arXiv:1905.04610

Lyngdoh GA, Zaki M, Krishnan NA, Das S (2022) Prediction of concrete strengths enabled by missing data imputation and interpretable machine learning. Cement Concr Compos 128:104414

Mahdevari S, Maarefvand P (2016) An investigation into the effects of block size distribution function on the strength of Bimrocks based on large-scale laboratory tests. Arab J Geosci 9(7):509

Medley EW (1994) The engineering characterization of melanges and similar block-in-matrix rocks (Bimrocks). University of California, Berkeley

Monjezi M, Mohamadi HA, Barati B, Khandelwal M (2014) Application of soft computing in predicting rock fragmentation to reduce environmental blasting side effects. Arab J Geosci 7(2):505–511

Müller M, Schwab N, Schickhoff U, Böhner J, Scholten T (2016) Soil temperature and soil moisture patterns in a Himalayan alpine treeline ecotone. Arct Antarct Alp Res 48(3):501–521

Nandy S, Adhikari M, Ray A, Rai R, Singh TN (2024) Edge-centric intelligent early warning system for residual soil stability prediction in slope. IEEE Internet Things J 11(3):3832–3839

Napoli ML, Barbero M, Scavia C (2021) Effects of block shape and inclination on the stability of melange Bimrocks. Bull Eng Geol Env 80(10):7457–7466

Napoli ML, Festa A, Barbero M (2022) Practical classification of geotechnically complex formations with block-in-matrix fabrics. Eng Geol 301:106595

Paliwal M, Goswami H, Ray A, Bharati AK, Rai R, Khandelwal M (2022) Stability prediction of residual soil and rock slope using artificial neural network. Adv Civ Eng 2022:4121193

Pan YW, Hsieh MH, Liao JJ (2008) Mechanical properties of virtual block-in-matrix colluvium. In: ARMA US rock mechanics/geomechanics symposium

Parsajoo M, Mohammed AS, Yagiz S, Armaghani DJ, Khandelwal M (2021) An evolutionary adaptive neuro-fuzzy inference system for estimating field penetration index of tunnel boring machine in rock mass. J Rock Mech Geotech Eng 13(6):1290–1299
Rabie AH, Mansour NA, Saleh AI (2023) Leopard seal optimization (LSO): a natural inspired meta-heuristic algorithm. Commun Nonlinear Sci Numer Simul 125:107338
Rahul, Khandelwal M, Rai R, Shrivastva BK (2015) Evaluation of dump slope stability of a coal mine using artificial neural network. Geomech Geophys Geo-energ Geo-resour 1:69–77
Ray A, Kumar V, Kumar A, Rai R, Khandelwal M, Singh TN (2020) Stability prediction of Himalayan residual soil slope using artificial neural network. Nat Hazards 103(3):3523–3540
Ray A, Bharati AK, Rai R, Singh T (2021) Landslide occurrences in Himalayan residual soil: a review. Himal Geol 42(1):189–204
Ray A, Verma G, Rai R, Singh T (2023) Stability assessment of Himalayan residual soil slopes formed from the weathering of carbonate lithologies using Landslide Hazard Charts. Himal Geol 44(2):71–88
Sonmez H, Gokceoglu C, Nefeslioglu HA, Kayabasi A (2006) Estimation of rock modulus: for intact rocks with an artificial neural network and for rock masses with a new empirical equation. Int J Rock Mech Min Sci 43(2):224–235
Sonmez H, Ercanoglu M, Kalender AYCAN, Dagdelenler G, Tunusluoglu C (2016) Predicting uniaxial compressive strength and deformation modulus of volcanic Bimrock considering engineering dimension. Int J Rock Mech Min Sci 86:91–103
Taylor KE (2005) Taylor diagram primer. Work Pap 1–4
Tyagi JV, Qazi N, Rai SP, Singh MP (2013) Analysis of soil moisture variation by forest cover structure in lower western Himalayas, India. J for Res 24:317–324
Verma G, Kumar B, Kumar C, Ray A, Khandelwal M (2023) Application of KRR, K-NN and GPR algorithms for predicting the soaked CBR of fine-grained plastic soils. Arab J Sci Eng 48(10):13901–13927
Wakabayashi J, Medley EW (2004) Geological characterization of melanges for practitioners. Felsbau 22(5):10–18
Xian-Wen H, Yao ZS, Bing-Hui W, Ai-Zhao Z, Jiang PM (2020) Soil-rock slope stability analysis under top loading considering the nonuniformity of rocks. Adv Civ Eng 2020:9575307
Zhang H, Nguyen H, Bui XN, Pradhan B, Asteris PG, Costache R, Aryal J (2022) A generalized artificial intelligence model for estimating the friction angle of clays in evaluating slope stability using a deep neural network and Harris Hawks optimization algorithm. Eng Comput 38:1–14
Zhou J, Shen X, Qiu Y, Shi X, Khandelwal M (2022) Cross-correlation stacking-based microseismic source location using three metaheuristic optimization algorithms. Tunn Undergr Space Technol 126:104570

Authors and Affiliations

Arunava Ray[1] · Gopika C. Atul[2] · Sanjog Chhetri Sapkota[3] · Prasenjit Saha[4] · Sourav Das[5] · Rajesh Rai[6] · Manoj Khandelwal[7]

✉ Manoj Khandelwal
m.khandelwal@federation.edu.au; mkhandelwal1@gmail.com

Arunava Ray
arunava.ray@vit.ac.in

Gopika C. Atul
gopika.catul2021@vitstudent.ac.in

Sanjog Chhetri Sapkota
kshetrisanjog@gmail.com

Prasenjit Saha
prasenjitsaha@iutripura.edu.in

Sourav Das
srv.das1@gmail.com

Rajesh Rai
rajeshrai.min@iitbhu.ac.in

[1] Centre for Disaster Mitigation and Management, Vellore Institute of Technology, Vellore, Tamil Nadu 632014, India

[2] Department of Civil Engineering, Vellore Institute of Technology, Vellore, Tamil Nadu 632014, India

[3] Department of Civil Engineering, Sharda University, Greater Noida, Uttar Pradesh 201306, India

[4] Department of Civil Engineering, ICFAI University, Tripura 799210, India

[5] Department of Civil Engineering, Barak Valley Engineering College, Karimganj, Assam 788701, India

[6] Department of Mining Engineering, IIT(BHU), Varanasi, Uttar Pradesh 221005, India

[7] Institute of Innovation, Science and Sustainability, Federation University Australia, Ballarat, VIC 3350, Australia